

## Automated 3-D Solid Rocket Combustion Stability Analysis

J.C. French\* & D.E. Coats†

Software & Engineering Associates, Inc., Carson City, NV

### Abstract

Solid rocket combustion stability analysis has historically focused on axial acoustic modes of vibration to predict motor stability. Although tangential modes of vibration have been observed during catastrophic motor failures, they have not been included in commonly used stability analysis computer codes, due to the increased complexity and computational requirements. In an effort to develop a multi-dimensional motor stability analysis code, and include new combustion instability drivers derived from the combustion instability MURI program, Software and Engineering Associates has assembled several computational tools that work in concert to predict motor stability. This suite of codes, when fully integrated, will generate a 3-D computational grid, perform a CFD analysis of the motor cavity's steady flow field, determine the multi-dimensional acoustic resonant mode shapes, and return stability parameters to the user. In this paper, our grid generator and acoustic mode eigensolver are presented along with several test cases. Together, these codes will form a new module in the JANNAF Solid Performance Program / Standard Stability Program (SPP/SSP) code set. The new module will be compatible with Spa's 3-D grain geometry input specification.

### Introduction

Solid rocket combustion instability is a potential problem in the development of any new solid rocket motor, and can arise even after the start of production. A solid rocket becomes unstable when the combustion processes couple with the acoustic modes of the chamber to increase the energy release in the chamber. To avoid costly post-production modifications, stability theories have been developed to predict whether or not an instability will occur for a given propellant, chamber geometry, ballistics and resonant mode.<sup>2-4</sup> These theories require the knowledge of the steady flow field, the acoustic mode shapes, the

unsteady rotational velocity field, and the propellant response.

Current design codes<sup>4,11,15</sup> are primarily one-dimensional, examining the combustion-acoustic interaction for solely axial waves. However, typical solid rocket motor grain designs often have multi-dimensional characteristics, affecting both the steady flow field and the acoustic modes. The stability equations<sup>2,12</sup> are written to account for fully 3-D geometries, but when the current design codes were written, the computers available had neither the speed nor the memory for practical evaluation of 3-D problems. Current computers can solve these problems in a reasonable amount of time, and the Navy has assigned Software and Engineering Associates, Inc. (SEA) the task to develop a stability analysis code that accounts for 3-D ballistics (steady flow field analysis) and 3-D acoustic modes (axial, tangential and radial).

The 3-D stability analysis will become part of the Standard Stability Prediction (SSP) code, and as such will be a module that may be executed by the Solid Performance Program (SPP) code. SPP provides the combustion chamber geometry and grain characteristics to the stability code. The stability code first generates a computational mesh of the motor cavity. The ballistics are then computed by a 3-D Euler CFD code, and the 3-D mode shapes are evaluated using an eigensolver. The CFD and acoustic modes are then used to compute the 3-D unsteady rotational velocity field. Parameters from the CFD, the acoustic modes and the unsteady rotational velocity field are then integrated over the chamber to predict the stability of the rocket motor. In this paper, we present the status of a wire frame code that can be generated from the SPP code, a mesh generator module, and an eigensolver to determine the acoustic mode shapes.

The approaches taken in this project have been limited by several criteria governing the desired final product. Any external code or program that is included in this suite of codes must be free in terms of both cost and distribution, (i.e., no licensed software and no distribution limitations), and the final product will be a module to be driven by SPP. Every maintained grid

---

Copyright 1999 by D.E. Coats. Published by the American Institute of Aeronautics and Astronautics, Inc. with permission.

\* Jonathan C. French, Senior Engineer, Member AIAA

† Douglas E. Coats, President, Associate Fellow AIAA

generation software code SEA found had some form of restriction placed upon it, forcing us to develop our own in-house code. The CFD coding began by implementing CFL3D (NASA code) to explore the problem, but due to its distribution restrictions and some inherent limitations (for example, CFL3D is hard coded for air), SEA has instead developed our own finite volume based Euler CFD code. To identify the acoustic mode shapes we used a public domain eigensolver<sup>8</sup>, which has advanced our progress tremendously.

### Mesh Generation

#### Wire Frame

To automate the grid generation, it was first necessary to define the motor grain surface. SPP contains information about the cavity, but not in an immediately useable form. SPP allows the user to specify geometrical primitives to define the initial motor cavity.<sup>9</sup> A primitive can be a prism, cone, sphere, or torus, and can be either a “grain filled” or a “void” region. The order in which the primitives are specified determines whether a grain filled primitive fills a void primitive, or if the void primitive hollows out the filled primitive. To burn back the grain, SPP then changes the size of the primitives (voids expand, grain filled contract), using appropriate corner rounding, to model the burning surfaces. Hercules first implemented this approach for ballistic computations<sup>13</sup>.

SPP contains routines that numerically integrate over cross sections of all the primitives at given axial locations, but the actual grain surfaces are never explicitly evaluated. It is possible to surmise a rough idea of the grain surface by examining the coding logic, but there are many potential pitfalls in “connecting the dots”, especially when considering that the grain can have fully 3-D characteristics. SPP does generate a non-structured surface mesh, but cannot handle double valued regions.

Due to these limitations, a completely general alternate option using a wire frame was chosen to evaluate the surface. The surface of each primitive is broken down into a series of polygons composed of triangles, squares and circles (each circle is approximated by an appropriate polygon). To determine the external surface, first every primitive’s polygons is compared with every other primitive’s polygons to find lines or planes of intersection. All intersections that occur for a given polygon are stored. Duplicate lines of intersection are removed. Then, every polygon is subdivided using the saved lines of intersection, and each sub-polygon is examined to check if it is on the surface. All of the sub-polygons on

the surface are saved, and after all of the polygons are processed the saved sub-polygons form a wire frame.

Figures 1.a-c demonstrate the burn back of the extended Delta<sup>14</sup> solid rocket motor grain. As the slots burn outward, they merge until they almost disappear (Fig. 1.c). These wire frames were created from an SPP generated data file and our wire frame code. A portion of the grain in Fig. 1.c is burnt out to the case.

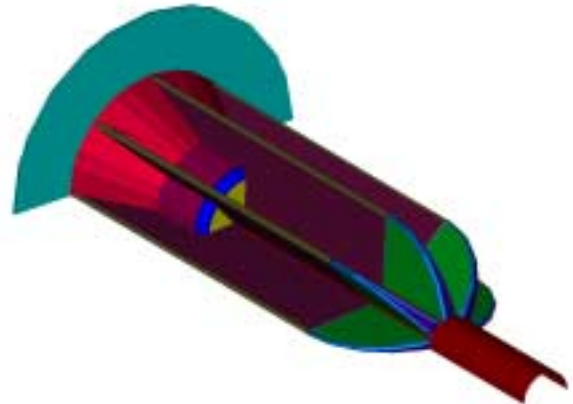


Figure 1.a. Initial extended Delta motor grain

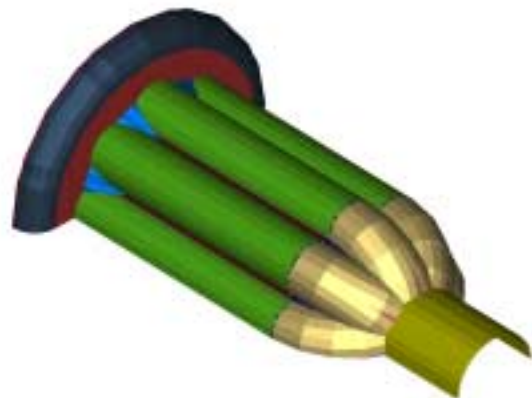


Figure 1.b. Extended Delta motor grain burnt back 2.5”

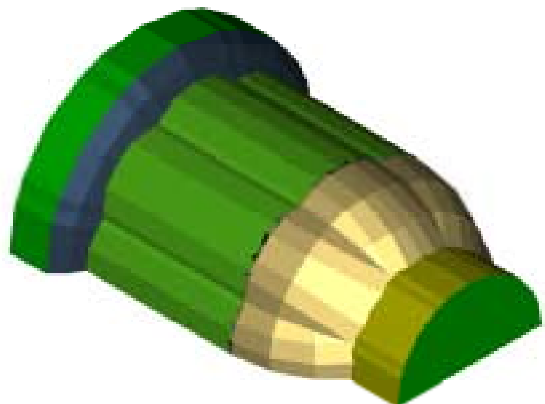
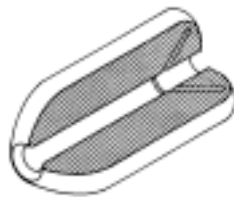


Figure 1.c. Extended Delta motor grain burnt back 8.0”

Trans-Finite Interpolation (TFI)/ Elliptic PDE Mesh Generation Methods

The general nature of the 3-D grains used in solid propellant rocket motors makes the task of automating the gridding of the void volume a formidable task. The problems associated with the gridding are increased with the requirement of gridding the void volume as the grain burns back.

The SPP97 computer code<sup>11</sup> is a super set of the JANNAF standard solid rocket motor performance analysis computer program<sup>9</sup>. The motor performance analysis module consists of a generalized 3-D grain design module coupled to an internal ballistics module. The automated grid generation procedures will be coupled to the grain design through the wire frame module, which describes the propellant surface. There are a number of standard grain design shapes that can be modeled in SPP97 using macros to help the user specify these shapes. Macros are defined for the Star, Wagon Wheel, Dogbone, Dendrite, Finocyl, and Conocyl shapes as shown in Fig. 2. These macros include a domes treatment, which allows a head end or aft end taper from one shape to another.



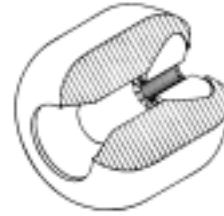
a) Conocyl



b) Dendrite



c) Wagon Wheel



d) Finocyl



e) Dogbone

Figure 2. Standard Grain Shapes

Almost all solid rocket motor grain shapes exhibit cyclic symmetry so that the entire void volume does not need to be modeled. For example, the Dendrite and Wagon Wheel shapes shown in Fig. 2.b and 2.c have 12 symmetry sections if mirroring is used. For center perforated motors, cylindrical coordinates represent the most convenient coordinate system. Hence at each axial station, the grid will be represented in the  $r-\theta$  coordinates instead of  $x$  and  $y$ .

To easily achieve second order accuracy for the CFD Euler solution, the use of body fitted coordinates with equal spacing in the transformed space is desired. Figure 3 shows the transition from  $x-y$  physical coordinates to  $r-\theta$  coordinates to transformed coordinates.

Multi-blocking of the regions to be gridded will be required for some grain geometries because of the complexity of the potential shapes. However, the current discussion will be limited to a single block at each axial station with the number of  $x-y$  grid points remaining unchanged down the length of the motor.

The two methods considered for this application are an algebraic method, transfinite interpolation (TFI), and a partial differential equation method, i.e., solution of elliptic partial differential equations (PDE). Both methods are well known and documented.<sup>1,10</sup>

### TFI Method

The TFI method is especially well suited for simple concave regions where it requires little user intervention to obtain an adequate grid. The basis for the method is the interpolation between the corresponding edges and an interpolation from each of the of the corner points (see Fig. 4). The simplest interpolation scheme is Lagrangian or linear, Eqn 1. Higher-order polynomial interpolation can be used to vary the grid spacing. Hermite polynomials are often used to force the grid lines to become perpendicular to the sides of the mesh. Fig. 5 gives an example of the use of both linear and Hermite polynomial interpolation for a simple star grain.

$$\mathbf{r}(\xi, \eta) = (1-\eta)\mathbf{r}_1(\xi) + \eta\mathbf{r}_2(\xi) + (1-\xi)[\mathbf{r}_3(\eta) - (1-\eta)\mathbf{r}_1(0) - \eta\mathbf{r}_2(0)] + \xi[\mathbf{r}_4(\eta) - (1-\eta)\mathbf{r}_1(1) - \eta\mathbf{r}_2(1)] \quad (1)$$

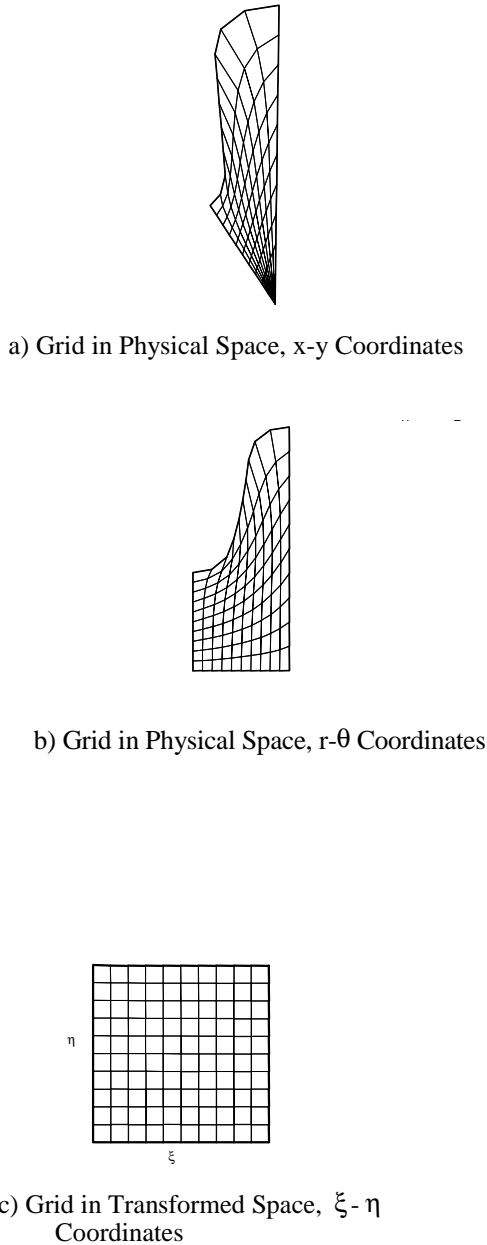


Figure 3. Coordinate Systems

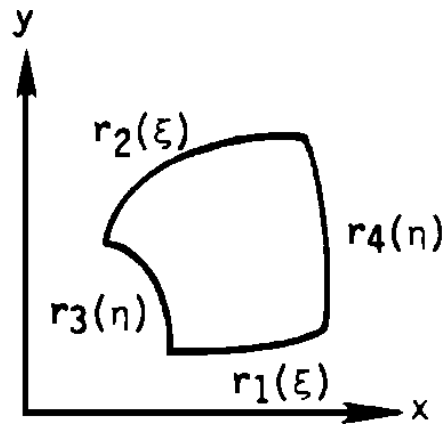
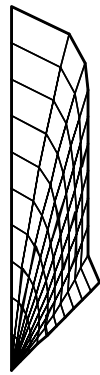
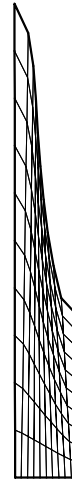


Figure 4. Domain For Transfinite Interpolation

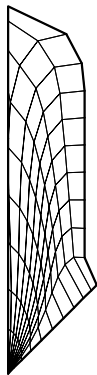
The use of higher order interpolation polynomials can lead to problems as can be seen in Fig. 5 c and 5.d. That is, some of the vertical grid lines are deflected too close to the boundary. In general, we have reached the conclusion that linear TFI is the most appropriate for the task at hand since it will require the least amount of user intervention. However, a Hermite polynomial interpolation option is also being provided to give the user added flexibility. It is anticipated that TFI will automatically be used only for simple grain shapes where its applicability can be predicted beforehand.



a) Linear Interpolation x-y Space



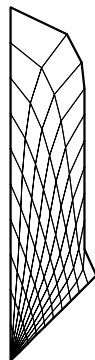
b) Linear Interpolation r-θ Space



c) Hermite Interpolation x-y Space



d) Hermite Interpolation r-θ Space



e) PDE Generated Grid, x-y Space



f) PDE Generated Grid, r-θ Space

Figure 5. TFI and PDE Generated Grids For a 2.75 Inch Motor Star Grain.

Elliptic partial differential equations methods have the property that the solutions are usually very smooth. If Laplace's equation is used, then the Jacobian is guaranteed to be positive due to the maximum principle for harmonic functions. However, for real situations, grid crossings are still a possibility due to finite mesh size and truncation error.

For our work, we have chosen Poisson's equation, Eqn. 2, to do the mapping between the physical and transformed space. The mapping is constructed by specifying the grid points on boundary of the physical space and the interior points calculated via the solution of Eqn. 2. The functions P and Q are terms that control the point spacing on the interior of the mesh. Inverting the dependent and independent variables allows us to write Eqn. 2 in terms of the physical space. Thus we have a system of two elliptic equations of the form

$$\begin{aligned}\xi_{xx} + \xi_{yy} &= P(\xi, \eta) \\ \eta_{xx} + \eta_{yy} &= Q(\xi, \eta)\end{aligned}\quad (2)$$

$$\begin{aligned}\alpha x_{\xi\xi} - 2\beta x_{\xi\eta} + \gamma x_{\eta\eta} &= -J^2(Px_{\xi} + Qx_{\eta}) \\ \alpha y_{\xi\xi} - 2\beta y_{\xi\eta} + \gamma y_{\eta\eta} &= -J^2(Py_{\xi} + Qy_{\eta})\end{aligned}\quad (3)$$

where

$$\begin{aligned}\alpha &= x_{\eta}^2 + y_{\eta}^2 \\ \beta &= x_{\xi}x_{\eta} + y_{\xi}y_{\eta} \\ \gamma &= x_{\xi}^2 + y_{\xi}^2 \\ J &= \frac{\partial(x, y)}{\partial(\xi, \eta)} = x_{\xi}y_{\eta} - x_{\eta}y_{\xi}\end{aligned}\quad (4)$$

The effect of the control functions P and Q is to cause lines of constant  $\eta$  to move in the same direction as the sign of Q and  $\xi$ -lines to deflect in the direction of the sign of P.

Numerical solution of 3 is straightforward and we used the coding of Thompson et al, in Ref. 10, which uses an over relaxation method to solve the PDE.

## Results

Both TFI and PDE methods were applied to a test motor geometry<sup>7</sup>. Figures 6 and 7 show the results of TFI and PDE grid generation down the motor axis. Because of the high angle formed by the star grain geometry, the TFI method yields results that are marginal at best.

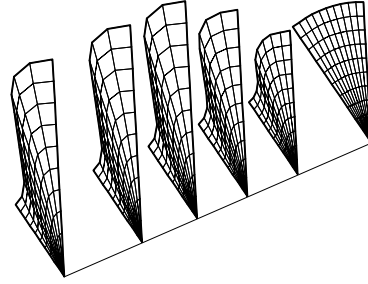


Figure 6. Sample Mesh Using TFI

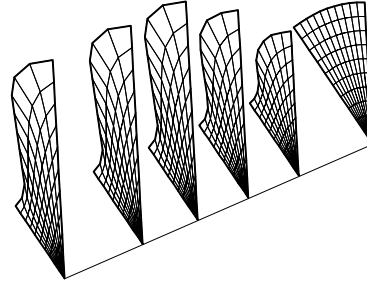


Figure 7. Sample Mesh Using PDE

## Acoustic Mode Shape Computation

In this paper, we compute the resonant frequencies and mode shapes by first establishing a system of equations which model the acoustics and appropriate boundary conditions, and then using an eigensolver determine the eigenvalues and eigenvectors (resonant frequencies & mode shapes) found within the equations. The system of equations is derived using the finite volume method to discretize the acoustic Helmholtz equation. This approach is significantly different from the approaches we have presented previously using the Green's Function Discretization (GFD) method<sup>6,7</sup>, and results from each approach are compared at the end of this section. An eigensolver can determine the eigenvalues and eigenvectors of matrix  $\overline{\overline{A}}$  ( $\overline{\phi}$  is the acoustic potential):

$$\overline{\overline{A}} \bullet \overline{\phi} + k^2 \overline{\phi} = 0 \quad (5)$$

Matrices are denoted by double over bars, and vectors are denoted by single over bars. In this case,  $\overline{\overline{A}}$  is not a function of k (the reduced frequency).

The GFD method solves

$$\overline{\overline{B}} \bullet \overline{\overline{\phi}} = \overline{\overline{e}} \quad (6)$$

directly over a range for values of  $k$  ( $\overline{\overline{e}}$  is a vector of random values).  $\overline{\overline{B}}$  is a non-linear function of  $k$ , so the eigenvalue problem cannot be formulated because the frequency parameter cannot be factored out. However, the overall system of equations that  $\overline{\overline{B}}$  represents is much more accurate than that of the finite volume approach. Instead of using an eigensolver, the GFD approach solves Equation 6 over a range of frequencies ( $k$ ), and saves the maximum field value of each solution for each  $k$ . Then the saved values are scanned to find resonant “peaks” corresponding to eigenvectors corrupting the particular solution. A better guess for  $k$  can then be made to hone in on the resonant frequency.

While the finite volume and eigensolver approach is less accurate than using GFD, the eigensolver approach is more easily automated and can be extended to work with multiple blocks of grids. Thus, we have chosen to examine this approach.

Several characteristics were considered while selecting a discretization method. The approach needed to be compatible with the eigenvalue formulation, flexible enough to handle corners and difficult geometries, and able to handle patching regions when the underlying computational grid changes abruptly. In addition, the method needed to be at least second order accurate to reduce the overall mesh requirements. Here we present a second order finite volume node-centered approach which meets these criteria. This derivation will be performed in 2-D, but the 3-D discretization follows directly from it.

For a 2-D 3x3 computational stencil, the conservation region is shown in Fig. 8, denoted by the dashed lines.

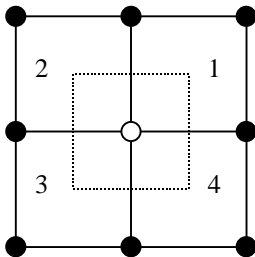


Figure 8. Finite volume computational stencil

In order to simplify the implementation of boundary conditions, this stencil is sub-divided into 4 quadrants, and the finite volume integration will be performed over each quadrant independently. Through this subdivision, if a particular quadrant is actually on the outside of the boundary, it can simply be ignored in the integration. For example, in Fig. 9 the boundary is

represented by the shaded block, leaving quadrants 2 and 3 “filled” with the boundary, so during the finite volume integration these quadrants can be ignored. Conceptually, the finite volume is reduced to the dashed region to the right of the vertical boundary line, and is closed by the vertical boundary line. The flux through the vertical boundary face is zero, due to the Neumann boundary condition. This effectively places the center node on the boundary.

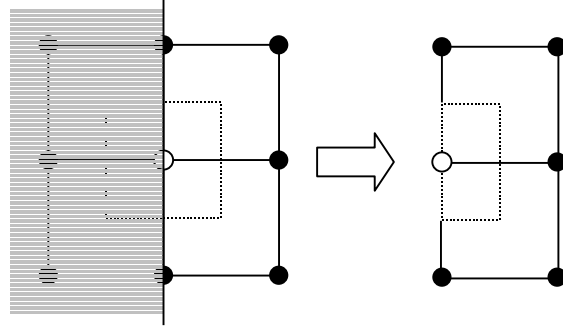


Figure 9. Finite volume computational stencil for node on boundary

To compute the finite volume discretization, first begin with the acoustic wave equation and associated hard wall (Neumann type) boundary condition ( $c$  is the speed of sound,  $t$  is a time parameter and  $\overline{n}$  is the boundary normal):

$$\frac{1}{c^2} \frac{\partial^2 \tilde{\phi}}{\partial t^2} = \nabla^2 \tilde{\phi} \quad (7)$$

$$\partial \tilde{\phi} / \partial \overline{n} = 0 \quad (8)$$

Assume the harmonic time variation ( $\omega$  is the natural frequency and  $L$  is a non-dimensionalizing length):

$$\tilde{\phi} = \phi e^{i\omega t} \quad (9)$$

$$\nabla^2 \phi + k^2 \phi = 0 \quad (10)$$

$$k = \omega L / c \quad (11)$$

This PDE is the acoustic Helmholtz equation. Take the area integral of the PDE over all four quadrants:

$$\iint [\nabla^2 \phi + k^2 \phi] dA = 0 \quad (12)$$

Each quadrant is integrated independently. Area  $A$  in Fig. C represents quadrant 1’s conservation region (see Fig. 8).

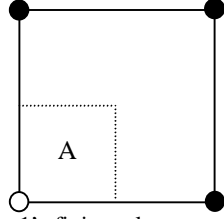


Figure 10. Quadrant 1's finite volume conservation region

Using Green's divergence theorem, reduce the first integrand to:

$$\oint \bar{n} \cdot \nabla \phi dL + k^2 \iint \phi dA = 0 \quad (13)$$

The line integral is taken only along the dashed lines.  $\bar{n}$  is the outward normal vector from along dashed sides of region A.

To compute the line integral along the dashed boundary in Fig. 10, it is necessary to approximate the gradient of the potential along each dashed line. To approximate the gradient along the vertical dashed line in Fig. 10, the gradient at the  $x$  is approximated as the average gradient over regions A and B in Fig. 11 [1, p.81]:

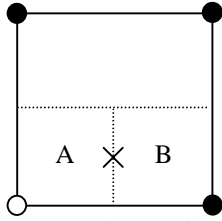


Figure 11. Quadrant 1 integration regions used to approximate a gradient

Let

$$C = A \cup B \quad (14)$$

The average gradient over area C is

$$\nabla \phi|_x \approx \frac{1}{C} \iint \nabla \phi dC \quad (15)$$

Apply Green's theorem a second time:

$$\nabla \phi|_x \approx \frac{1}{C} \oint \bar{n}_C \phi dL_C \quad (16)$$

This line integral is evaluated around region C.  $\bar{n}_C$  is the outward normal from region C, and  $L_C$  is the line around region C. Thus, by integrating around region C, the average value of the gradient of phi at the center of C can be determined without taking any explicit differences. The value of  $\hat{\phi}$  along each edge is

approximated by averages of  $\phi$  from the corners of the quadrant at the  $x$ 's. Fig. 12 shows the average  $\hat{\phi}$  locations.

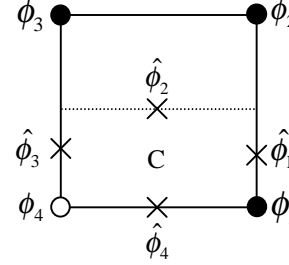


Figure 12. Corner node and average value  $\hat{\phi}$  locations

$$\begin{aligned} \hat{\phi}_1 &= (3\phi_1 + \phi_2)/4 \\ \hat{\phi}_2 &= (\phi_1 + \phi_2 + \phi_3 + \phi_4)/4 \\ \hat{\phi}_3 &= (\phi_3 + 3\phi_4)/4 \\ \hat{\phi}_4 &= (\phi_1 + \phi_4)/2 \end{aligned} \quad (17)$$

This process is repeated to compute the average gradient for the horizontal dashed line in Fig. 10. Note that only values from this quadrant are used. This significantly simplifies the discretization process for evaluating both convex and concave corners, as the quadrants that are outside the boundary can be ignored without requiring special considerations for the evaluation of the fluxes in the quadrants inside the boundary.

The area integral in Equation 13 is approximated by the value at the center of the stencil multiplied by the total area of the used quadrant's conservation regions. A better approximation can be computed using the sum of the average values of the acoustic potentials over each conservation region, but the small additional accuracy gained would have resulted in a doubling of the memory requirements, and as such was not warranted.

To extend this approach to a 3-D 3x3x3 stencil, eight quadrants are used, and in each quadrant three surfaces (and three corresponding gradients) are evaluated. Volume integrals replace area integrals, and area integrals replace the line integrals.

The resulting system of equations is non-symmetric, and if a structured set of nodes is used, banded. The eigensolver package ARPACK is a free eigensolver package that can evaluate non-symmetric banded matrices, using the implicitly restarted Arnoldi method<sup>8</sup>. ARPACK uses the somewhat inefficient but general LAPACK band form. After substituting a less

general but packed banded matrix structure, both memory requirements and matrix operation time was significantly reduced. The new matrix structure is packed to the extent that it has only 27 columns (corresponding to the 3x3x3 computational stencil).

For the general eigenvalue problem, the only  $\bar{A}$  matrix operation that ARPACK utilizes and the only time the matrix is referenced is the matrix dot vector  $(\bar{A} \cdot \bar{\phi})$  operation. This allows the user to easily specify the most appropriate matrix structure for a given problem

To compare the accuracy of the GFD and finite volume methods, both methods were used to compute the first 30 mode shapes for a cylinder with length of one and a radius of 0.321. The cylindrical geometry is shown in Fig. 13.

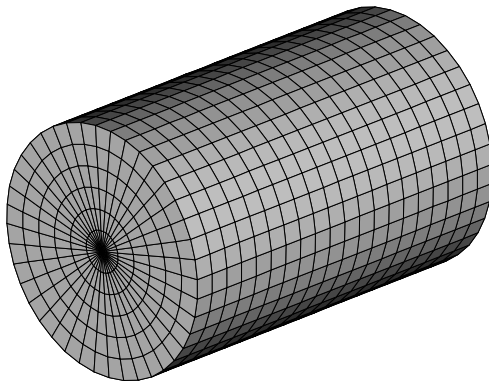


Figure 13. Cylindrical computational grid

Two computational grids were used. The first grid has 21 nodes in the axial direction, 7 nodes in the radial direction and 40 nodes in the theta direction. The second grid has 41 nodes axially, 13 nodes radially and 80 nodes in the tangentially (twice as dense as the first grid). The GFD method was used to evaluate the resonant frequencies using the coarse mesh, and the finite volume method was used to evaluate the resonant frequencies on both grids. The relative errors for all the methods and each mode are shown in Table I. In the mode column, Ax stands for the  $x^{\text{th}}$  axial mode, Tx stands for the  $x^{\text{th}}$  tangential mode and Rx stands for the  $x^{\text{th}}$  radial mode. The final column of Table I is the coarse grid's error divided by the fine grid's error. By doubling the grid density, the accuracy in evaluating the resonant frequencies was improved by a factor of four, implying that this finite volume discretization has second order accuracy.

Mode	Relative Error in k (%)			Ratio FV Error
	GFD	Finite Volume	2x Finite Volume	
A1	0.00016%	0.10%	0.026%	3.99
T1	0.00009%	0.25%	0.064%	4.00
A2	0.00170%	0.41%	0.103%	4.00
A1 T1	0.00040%	0.44%	0.111%	4.00
A2 T1	0.03719%	0.90%	0.255%	3.55
A3	0.01151%	0.92%	0.231%	3.99
T2	0.00005%	0.75%	0.187%	4.00
A1 T2	0.00016%	0.93%	0.234%	3.99
A3 T1	0.00010%	1.44%	0.363%	3.98
A2 T2	0.00010%	1.42%	0.355%	3.99
R1	0.02003%	1.36%	0.346%	3.94
A1 R1	0.02076%	1.56%	0.395%	3.94
A4	0.00901%	1.64%	0.411%	3.99
T3	0.00099%	1.56%	0.388%	4.02
A3 T2	0.00016%	2.09%	0.525%	3.98
A1 T3	0.00108%	1.74%	0.434%	4.01
A2 R1	0.00856%	2.07%	0.526%	3.94
A4 T1	0.00007%	2.19%	0.551%	3.97
A2 T3	0.00111%	2.24%	0.560%	3.99
A3 R1	0.01554%	2.81%	0.714%	3.93
A5	0.01028%	2.55%	0.641%	3.98
A4 T2	0.00010%	2.91%	0.734%	3.96
T4	0.00003%	2.59%	0.645%	4.02
T1 R1	0.00127%	2.65%	0.668%	3.97
A5 T1	0.00007%	3.12%	0.786%	3.96
A1 T4	0.00007%	2.77%	0.691%	4.01
A1 T1 R1	0.00124%	2.84%	0.716%	3.97

Table I. GFD and finite volume method accuracy comparison for the first 30 resonant frequencies of a cylinder

In contrast to GFD approach, the eigensolver approach yields an orthogonal set of mode shapes, and this is helpful in distinguishing different mode shapes that have the same frequency. For example, tangential modes can be reduced to the sum of two distinct standing wave patterns with the same frequency. For cylinders, the sine and cosine functions provide a set of distinct mode shapes. For slotted chambers with an even number of slots, the waves tend to bounce across the diameter and form symmetric patterns. However, chambers with an odd number of slots should have two very different tangential mode shapes.

To verify this, Fig. 14 contains a test case previously examined in [7], a chamber with five slots which tapers into a circle. The amplitudes of the 24<sup>th</sup> axial mode are plotted Fig. 15 (axially compressed for detail). Figure 15 also shows the computational mesh used.



Figure 14. Test motor chamber grid (to scale)

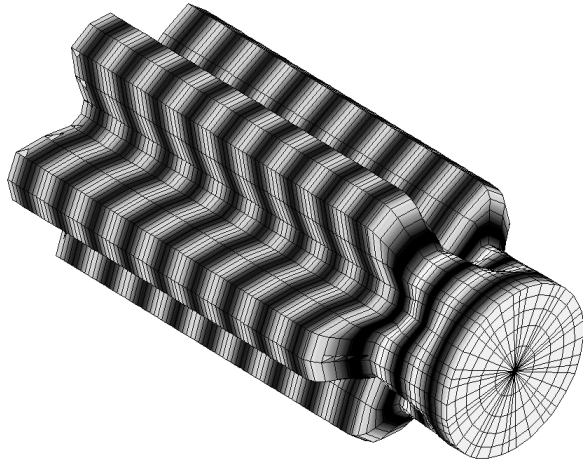


Figure 15. Test motor chamber's 24<sup>th</sup> axial mode (contoured with shading)

The first tangential mode for this chamber occurs immediately after the 24<sup>th</sup> axial mode (Fig. 16). Note in Fig. 16 that the first tangential mode does not enter the region with the smaller radius – this verifies observations made in liquid motor studies. Two different tangential modes with the same frequency are shown in Figs. 17.a and 17.b. The horizontal line in the figures is the periodic boundary of the otherwise Cartesian grid. Note in Fig. 17.a the node line occurs along the length of a single slot (along the periodic boundary), and the wave bounces in the vertical direction. This corresponds to a cylindrical geometry's sine wave motion. However, in Fig. 17.b the node line (highlighted) connects the grain's peaks, and the wave bounces in the horizontal direction with a maximum peak in the rightmost leg, and this corresponds to a cylindrical geometry's cosine wave motion.

The resonant frequency that occurs after the first tangential frequency corresponds to the first tangential and first axial mixed mode (Fig. 18). For illustrative purposes, the first tangential and eighth axial mode is shown in Fig. 19.

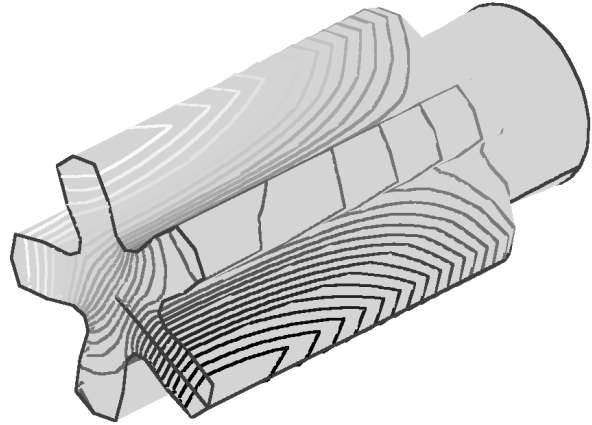


Figure 16. Test motor chamber's first tangential mode (contoured with lines)

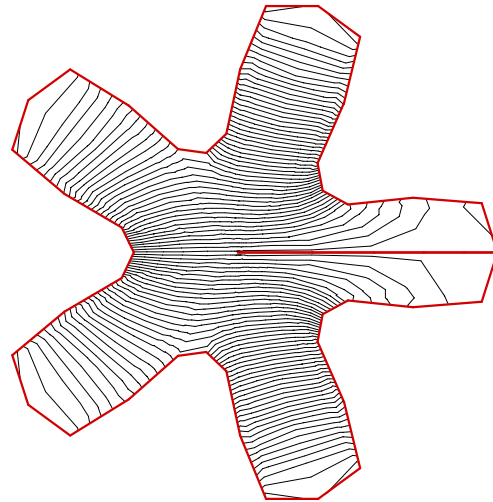


Figure 17.a. Five slot first tangential mode, horizontal node line into slot

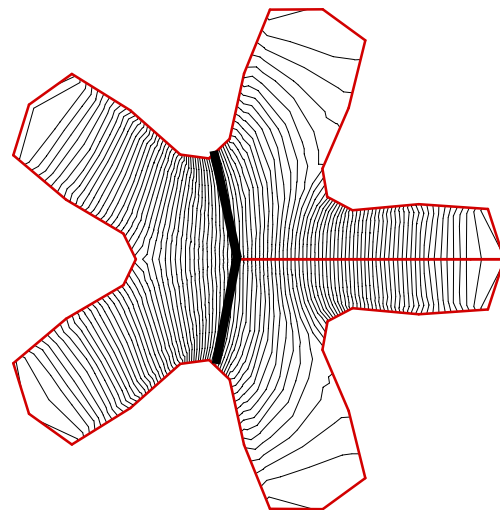


Figure 17.b. Five slot first tangential mode, vertical node line (highlighted)

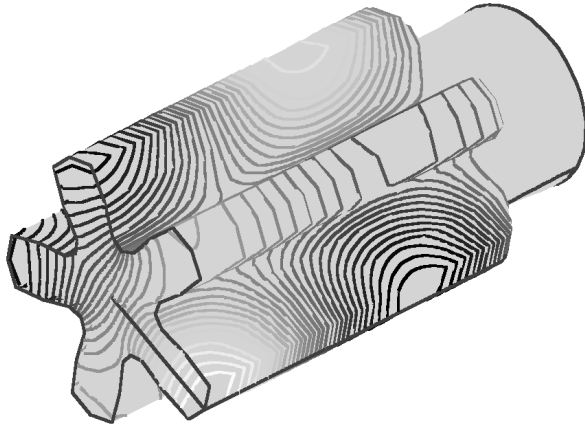


Figure 18. Five slot first tangential & first axial mixed mode (contoured with lines)

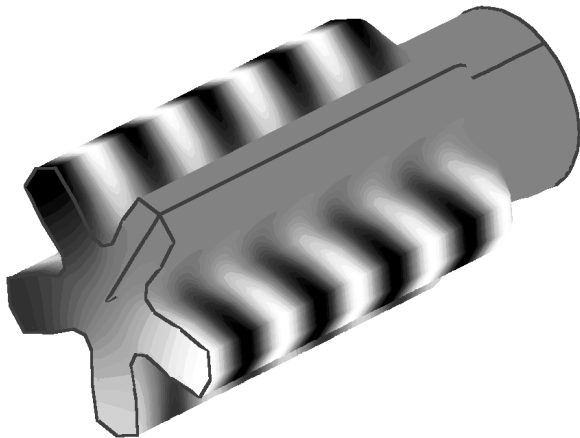


Figure 19. Five slot first tangential & 8<sup>th</sup> axial mixed mode (contoured with shading)

## Conclusions and Future Work

### Wire Frame

It is possible to generate a wire frame from the SPP97 geometric primitive data. The wire frame code is still being tested to verify that it can handle complicated geometries. An interface is needed to transmit a wire frame's surface information to the mesh generator.

### TFI / PDE Mesh Generation Methods

Efforts at automating the grid generation of solid rocket motor cavities have resulted in the following conclusions about future work:

1. Multiblocking will be required for many grain shapes.

2. Strategies for automatic grid generation can be worked out for particular grain designs only.
3. TFI can be used for simple concave regions. The criteria currently being considered for TFI use is that the grain slope in the  $r-\theta$  space be less than  $45^\circ$ .
4. PDE generated grids are the most robust in terms of minimum user intervention. Strategies for selecting values of P and Q for specific grain designs will have to be developed.

### Acoustic Mode Shape Computation

Two very different approaches to determining the acoustic mode shapes are presented. GFD is extremely accurate, requires fewer computational nodes, and it is easy to implement sub-grid boundary information. However, in contrast to GFD, the finite volume and eigensolver approach returns the resonant frequencies and mode shapes directly, without iteratively searching for each mode, which simplifies the mode shape determination. Also, if a specific frequency corresponds to two different mode shapes, the eigensolver identifies both mode shapes, which is especially important in the evaluation of tangential modes. For these two reasons, we plan to implement the finite volume / eigensolver approach in the stability module.

It would have been possible to implement a finite element approach instead of using the finite volume method. However, our CFD analysis uses the finite volume method, and it is easier to put a finite volume equations into a highly packed block matrix form.

The current code needs to be modified to handle blocks of grids in order to be compatible with a mesh generated for the CFD analysis.

### Acknowledgements

The authors would like to thank Dr. Fred Blomshield, of the China Lake Naval Air Warfare Center, for his continuing support of this SBIR effort. We would also like to acknowledge the work done at Rice University by Rich Lehoucq, Kristi Maschhoff, Danny Sorensen and Chao Yang in developing and maintaining the ARPACK eigensolver package (<http://www.caam.rice.edu/software/ARPACK>).

## References

- [1] Tannehill, J.C., Anderson, D.A., Pletcher, R.H., "Computational Fluid Mechanics and Heat Transfer, 2<sup>nd</sup> Edition", Taylor & Francis, Washington, DC, © 1997.
- [2] Flandro, G.A., "Effects of Vorticity on Rocket Combustion Stability," *Journal of Propulsion and Power*, 1995, vol. 11(4).
- [3] Culick, F.E.C., "Stability of Longitudinal Oscillations with Pressure and Velocity Coupling in a Solid Propellant Rocket," *Combustion Science and Technology*, 1970, vol. 2, pp. 179-201.
- [4] Dudley, D.P., Waugh, R.C., "Standardized Stability Prediction Methods for Solid Rocket Motors, Vol. II, Multidimensional Computer Program User's Manual," Aerojet Solid Propulsion Company, AFRPL-TR-76-32, May 1976.
- [5] French, J.C., Flanagan, S.N., and Flandro, G.A., "A New Method for Combustion Instability Mode Shape and Frequency Computations," JANNAF Propulsion Conference, Monterey, CA, November 1996.
- [6] French, J.C., "Three Dimensional Combustion Stability Modeling for Solid Rocket Motors", 34<sup>th</sup> AIAA / ASME / SAE / ASEE Joint Propulsion Conference, AIAA paper 98-3702, Cleveland, OH, July 1998.
- [7] French, J.C., Dang, A.L., "Analytic Combustion Stability Analysis of a Non-Axi-Symmetric Motor Cavity, Including Non-Axial Acoustic Modes: A Status Report", JANNAF Propulsion Conference, Tucson, AZ, December 1998.
- [8] Lehoucq, R.B., Sorensen, D.C., Yang, C., "ARPACK Users' Guide: Solution of Large Scale Eigenvalue Problems with Implicitly Restarted Arnoldi Methods", available at <http://www.caam.rice.edu/software/ARPACK>, Oct. 1997.
- [9] Nickerson, G.R., Dunn, S.S., Berker, D.R., "The Solid Propellant Rocket Motor Performance Prediction Computer Program (SPP), Version 7.0", AFAL-TR-87-078 Vol. 7, Final Report, February 1992.
- [10] Thompson, J.F., Warsi, Z.U., Mastin, C.W., "Numerical Grid Generation", North Holland, New York, © 1985.
- [11] Lovine, R.L., Waugh, R.C., "Standardized Stability Prediction Method for Solid Rocket Motors, Vol. III, Axial Mode Compute Program User's Manual", Aerojet Solid Propulsion Company, AFRPL-TR-76-32, May 1976.
- [12] Culick, F.E.C., "Stability of Three-Dimensional Motions in a Combustion Chamber", *Combustion Science and Technology*, Vol. 10 (1975) pp. 109-124.
- [13] Barron, J.G., Jr; Cook, K.S., Johnson, W.C., "Grain Design and Internal Ballistics Evaluation Program (IBM 7094 FORTRAN IV), Program No. 64101 (AD 818321), Hercules Powder Co., Bacchus Works (Magna, UT), July 1967.
- [14] Thiokol Chemical Corp., Elkton Division, Elkton, Maryland, "TE-M-364-4 Extended Delta Rocket Motor", Final Report, NASA Contract NAS7-678, 1972.
- [15] Nickerson, G.R., Culick, F.E.C., Dang, A.L., "The Solid Propellant Rocket Motor Performance Prediction Computer Program (SPP), Version 6.0", AFAL-TR-87-078 Vol. 6, October 1987.
- [15] Dunn, S.S., Coats, D.E., Nickerson, G.R., "SPP97 User's Manual", SEA Report 97-2, 1997.